2017 M_w 8.1 Tehuantepec Earthquake: Deep Slip and Rupture Directivity Enhance Ground Shaking but Weaken the Tsunami

by Kejie Chen, Wanpeng Feng, Zhen Liu, and Y. Tony Song

ABSTRACT

The 8 September 2017 M_w 8.1 Tehuantepec normal-faulting earthquake caused unexpected widespread intensive shaking, strongly felt as far as Mexico City about 720 km northwest of the epicenter, and generated a 1.8 m tsunami at the coast. Just 11 days later, another devastating M_w 7.1 Puebla earthquake occurred near Mexico City. In this contribution, we characterized this event by a joint inversion using static Global Positioning System (GPS) offsets, Interferometric Synthetic Aperture Radar (InSAR) measurements, high-rate GPS, and teleseismic displacement waveforms, then validated the preferred model by tsunami observations. We demonstrate that the Tehuantepec earthquake rupture propagates mainly unilaterally toward the northwest at a relatively high speed (~3.4 km/s), with three asperities identified: the dominant one is centered between depths from ~40 to 60 km while the other two are located at shallower (~20 km) and deeper (~90 km) depths, respectively. Moreover, we find the peak ground acceleration (PGA) recorded along the rupture propagation direction is much larger than that recorded at stations in the opposite direction with nearly identical epicentral distances (~700 km). Dynamic displacements reaching 5 cm were also observed at a GPS station ~1450 km from the epicenter. Based on these observations and our model results, we suggest that the deep slip in the low-attenuation mantle and the rupture directivity likely enhance the nationwide ground shaking, whereas the shallow slip may contribute to the local tsunami heights. The derived slip distribution is valuable for future investigation on the explicit relationship between the M_w 8.1 Tehuantepec and M_w 7.1 Puebla events.

Electronic Supplement: Figures of epicenter location, Global Positioning System (GPS) displacement waveform fits, trade-off between data fits, map view of the slip distribution and static GPS offset fits, observed and synthetic Interferometric Synthetic Aperture Radar (InSAR) data and residuals, distribution of teleseismic stations and waveform fits, distribution of deep-ocean assessment and reporting of tsunami (DART) buoys and near coastal tide gauges, cross-section view of Slab 1.0, coseismic displacement waveforms, tsunami predictions, and movie of the space–time history of the rupture propagation.

INTRODUCTION

Shortly after the catastrophic 1985 M_w 8.0 Mexico City earthquake that killed up to 50,000 people, the Mexican Seismic Alert System (Spanish: Sistema de Alerta Sísmica Mexicano [SASMEX]) was installed and in full operation by 1993, in order to provide earthquake warning within 60 s for portions of central and southern Mexico (Aranda *et al.*, 1995). During the normal-faulting M_w 8.1 earthquake (Fig. 1), which struck off the Chiapas coast of southern Mexico at approximately 23:49 local time on 7 September (04:49 on 8 September UTC) 2017 (see Data and Resources), SASMEX alerted Mexico City, about 720 km away from the epicenter, within two minutes (Suárez *et al.*, 2018). Generally, the most intense ground motions will occur close to the rupturing fault and attenuate quickly as one moves away from the fault. In this event, while the most affected regions are the near-epicenter southern states of Oaxaca, Chiapas, and Tabasco - where 98 people were killed and more than 300 people were injured - the shaking was also widely felt by 50 million people over the country, and unexpectedly caused building damage and prompted mass evacuations as far as Mexico City.

In addition, the submarine earthquake also generated a local tsunami of 1.75 m at the coast, and a tsunami alert was issued (see Data and Resources). Previous studies mainly focus on tsunamis triggered by megathrust earthquakes, such as the 2004 Sumatra, Indonesia; 2011 Tohoku, Japan; and 2015 Illapel, Chile, cases (see e.g., Sobolev *et al.*, 2007; Melgar and Bock, 2013; Chen, Babeyko, *et al.*, 2016). In contrast, records of tsunamis caused by normal-faulting ruptures are not common. One normal-faulting tsunamigenic case is the 2009 M_w 8.1 Samoa earthquake. However, as shown by Beavan *et al.* (2010) and Lay *et al.* (2010), the 2009 Samoa event is complicated by a nearly simultaneous M_w 8 thrust rupture in the shallow subduction interface, and it has not been quantified to

doi: 10.1785/0220170277

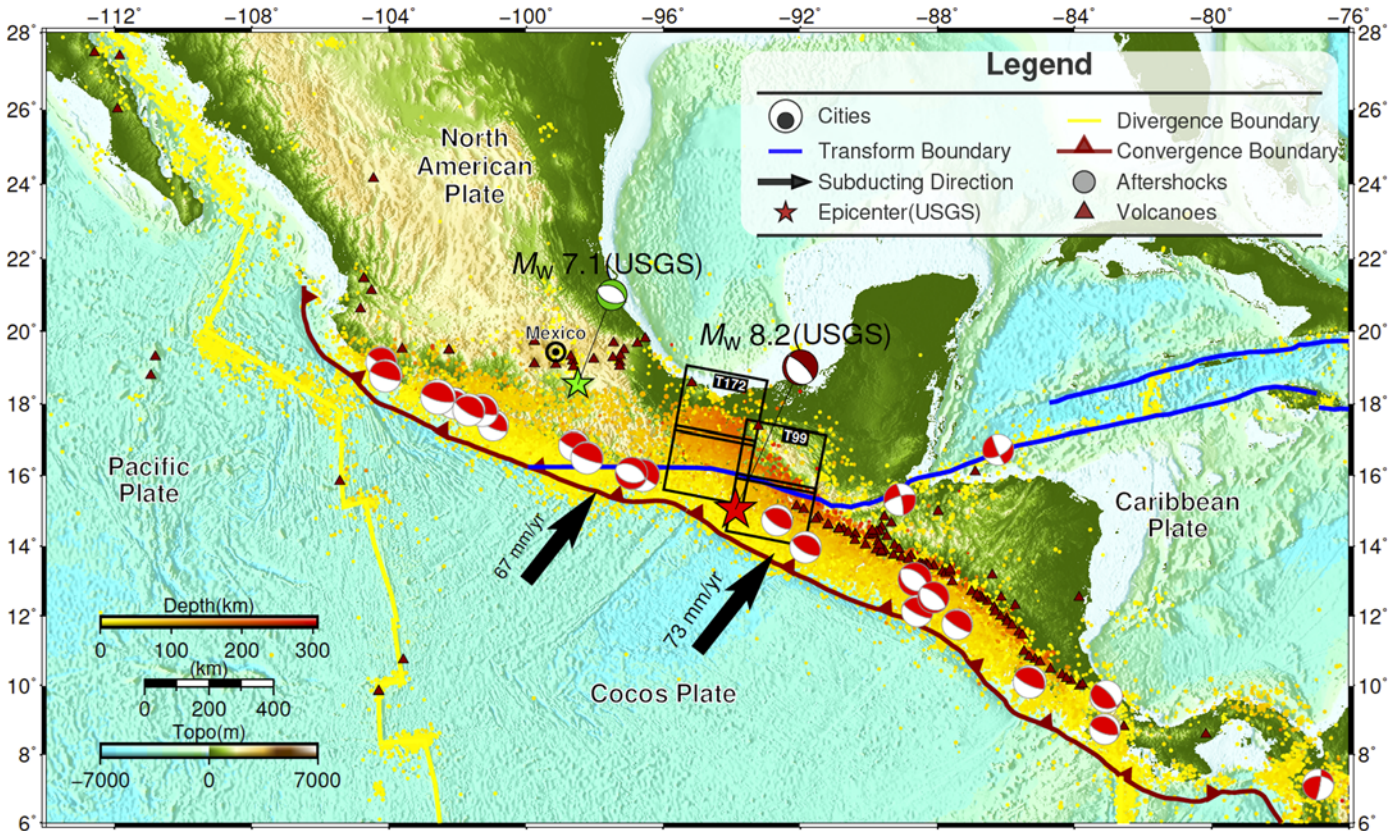

▲ **Figure 1.** Tectonic settings and historical seismicity in the region of the 2017 M_w 8.1 earthquake. Focal mechanisms plots are from Global Centroid Moment Tensor (CMT), the M_w 7.1 Puebla earthquake normal-faulting event occurred on 19 September 2017, 11 days after the mainshock. The plate boundaries are based on global plate model PB2003 (Bird, 2003). USGS, U.S. Geological Survey. The color version of this figure is available only in the electronic edition.

which degree the normal faulting accounts for the final tsunami amplitude. Therefore, the tsunami generated by pure normal earthquakes remains unclear and deserves further study.

Just 11 days later, the M_w 7.1 Puebla earthquake (Fig. 1) occurred in central Mexico, about 650 km northwest of the Tehuantepec earthquake (see Data and Resources). The second earthquake caused 370 deaths and injured about 6,000 people. Many buildings were reduced to rubble in the states of Puebla, Morelos, and Guerrero, as well as in Mexico City. Naturally, the question of whether the two earthquakes are linked is raised among scientific community (Segou and Parsons, 2018). In this regard, it is important to have source models for the events to explore the possible relationships for seismic hazard mitigation in the future.

Tectonically, the Tehuantepec earthquake fills in one of the previously identified seismic gaps along the Middle American subduction zone (MASZ; Wang *et al.*, 1982). Three major tectonic plates such as the Cocos, North American, and Caribbean planes intersect near the epicenter (Fig. 1) (Bird, 2003). Local tectonic structures in the region are not well understood yet. An inland volcanic arc was broken up at N15° along MASZ near the 2017 mainshock (Fig. 1), suggesting a possible lateral variation of geothermal processes at depth along the segment of MASZ. A very shallow dipping subduction interface along the profile crossing Mexico City was previously suggested based on seismic tomography study (Payero *et al.*, 2008). This could explain why a volcanic arc parallel to the trench is absent along the northern coast of Mexico. However, no detailed tomography observations were made in the area of the 2017 mainshock.

This largest recorded normal-faulting event provides us an opportunity for better estimates of how intense shaking and tsunami potential will be during future similar earthquakes. To better understand the seismogenic environment of the earthquake and its implication for seismic-related nature hazard prevention, we first perform a joint inversion to construct a seismic source model of the 2017 Tehuantepec earthquake using 1-Hz Global Positioning System (GPS) displacement waveforms, static GPS offsets, Interferometric Synthetic Aperture Radar (InSAR) observations, and teleseismic *P* waves in this study. We show a kinematic slip model of the mainshock, which offers us an insight into the Mexican tectonic complex. The model is then validated by tsunami observations and ground-motion records. We also explore the possible relationship between M_w 8.1 Tehuantepec earthquake and M_w 7.1 Puebla aftershock. Finally, we discuss its implications for future tsunami and earthquake hazard mitigation.

DATA AND METHODS

We utilize raw high-rate (1 Hz) GPS observations at 16 stations (Fig. 2) from the Nevada Geodetic Laboratory (NGL; see Data and Resources) and use precise point positioning technique to obtain high-rate displacement waveform solutions with centimeter accuracy through Positioning and Navigation Data Analyst software. Data processing strategies are the same as shown in Chen, Ge, *et al.* (2016). The positions retrieved are aligned to International Terrestrial Reference Frame 2008 and transformed into a local north, east, and up frames. The displacement waveforms at four of the stations show no appreciable coseismic offsets and are excluded from the inversion; we confirm through a sensitivity test that these stations provide no value to the slip inversion.

Coseismic static offsets at 70 GPS stations sampled at 30 s (see Ⓔ Fig. S3, available in the electronic supplement to this article) are provided by NGL through differencing the average station positions ten days before and two days after the event. Offsets at three other near-field GPS stations (OXTH, OXPE, and TNPJ), which have a data gap before the event, were estimated based on the time series (see Data and Resources) prepared by NGL instead. The maximum horizontal offset is about 13 cm southward at OXTH with ~200 km epicentral distance, while measurable offsets (~0.7 cm) are also observed as far east as the Yucatan Peninsula ~1000 km from the epicenter.

Two Sentinel-1 Terrain Observation by Progressive Scans (TOPS) tracks of Synthetic Aperture Radar (SAR) data from the European Space Agency (ESA) are processed for mapping coseismic displacements associated with the 2017 M_w 8.1 Tehuantepec earthquake mainshock. The InSAR processing is conducted with an automated InSAR processing system developed at the Canada Center for Mapping and Earthquake observations (Feng *et al.*, 2016; Feng, Tian, *et al.*, 2017). Several adjacent frames of TOPS data in each track are stitched together to fully cover the deformation area associated with the mainshock. The 90-m Shuttle Radar Topography Mission digital elevation model is used for coregistration and topographic phase removal in the InSAR processing (Farr *et al.*, 2007). Multilooking numbers of 20 and 4 are applied for the range and azimuth directions of the SAR data, respectively. To avoid effects of obvious atmospheric signals in track 99 (Fig. 1), we cropped out the maximum deformation area only in the geocoded unwrapped phase of track 99 before data downsampling. Finally, 2714 and 1800 points are used in the inversion from tracks 172 and 99, respectively.

The static GPS and InSAR data cover periods from 29 August to 10 September and 2 September to 20 September, respectively. During the time span after the mainshock, we have a total of 335 aftershocks, in which the largest aftershock is smaller than M_w 6. The total seismic moment released from the aftershocks is 5.438×10^{18} N · m, equivalent to M_w 6.5. This is smaller than 1/400 of the seismic moment of the mainshock. Obviously, we can fully neglect the effects of aftershocks in the static GPS and InSAR coseismic modeling.

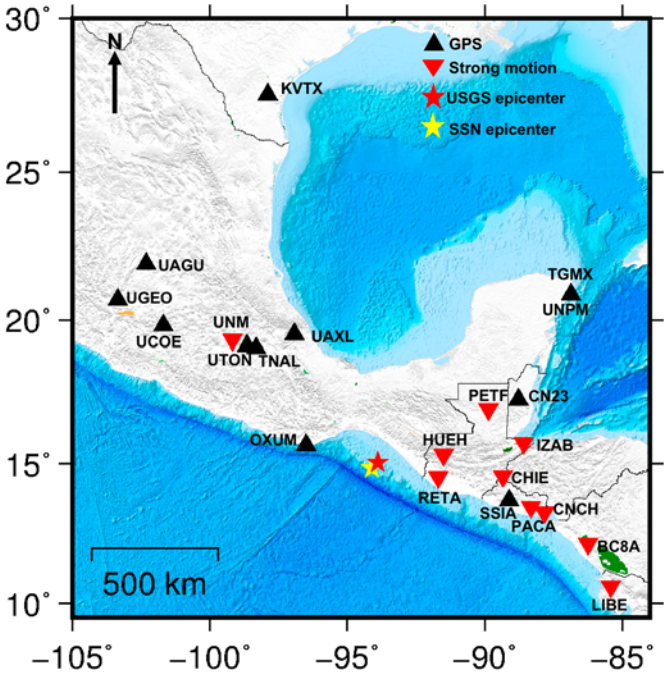

▲ **Figure 2.** Epicenter location determined from National Seismological Service of Mexico (SSN) and USGS (stars). Triangles and inverted triangles represent 1-Hz Global Positioning System (GPS) and strong-motion stations, respectively. The color version of this figure is available only in the electronic edition.

Broadband teleseismic *P*-wave displacements at 36 stations (see Ⓔ Fig. S5) with epicentral distances ranging from 30° to 90° are downloaded from the Incorporated Research Institutions for Seismology (IRIS) data center for the finite source inversion. The ground displacement waveforms are filtered with a band-pass filter with corner frequencies of 0.005–0.4 Hz and decimated to 1 Hz. A 120-s-long time window is extracted from the raw data, starting 6 s prior to the clearest first arrival of the *P* waves, and the *P*-wave initial motions are aligned manually to the theoretical arrival time inferred from preliminary reference Earth model (PREM; Dziewonski and Anderson, 1981).

With respect to the precision of hypocenter locations that can significantly affect the final slip model (Zhang *et al.*, 2012), we notice that there is a significant difference between solutions from the National Seismological Service of Mexico (SSN) ([94.11° W, 14.85° N] at depth 58 km) and the U.S. Geological Survey (USGS) ([93.899° W, 15.022° N], at depth 47.4 km) (see Fig. 2). Considering that the local 1-Hz GPS displacement waveforms are very sensitive to hypocenter location in slip inversion, we first test the two hypocenter locations through slip inversion using only 1-Hz GPS data and find the data fit based on the SSN hypocenter solution is much better than that from the USGS hypocenter (see the results in Ⓔ Fig. S1). As a result, we adopt the SSN hypocenter in our inversion.

We start with an initial fault geometry based on the SSN hypocenter and geometry parameters in the SSN focal mechanism (strike 311, dip 84, and rake −94). We discretize the fault

into 30 subfaults in the strike direction and 10 subfaults in the dip with 10×10 km^2 for each fault patch. The source time function of the each subfault is parameterized with five symmetric triangles with 3-s half-durations staggered by 1.5 s each. To further estimate optimal geometric parameters of the earthquake fault, in the inversion procedure we perform a grid search for strike, dip, and rake angle with a searching range by adding $\pm 10°$ to the initial value with 1° step. For each fault patch, two orthogonal slip vectors, defined based on the preferential rake angle, are used and nonnegative least-squares inversion is employed to allow a rake-varying slip (Hartzell *et al.*, 2007; Zhang *et al.*, 2009). We use the frequency–wavenumber integration method (Zhu and Rivera 2002) to compute Green's functions for static GPS and InSAR offsets and 1-Hz GPS displacement waveforms using a 1D layered velocity model from Santoyo *et al.* (2005). The teleseismic Green's functions are generated with a propagator matrix approach (Kikuchi and Kanamori, 1982). We adopt the aforementioned 1D layered velocity model for the source side and PREM (Dziewonski and Anderson, 1981) for the receiver side. The same band-pass filter used for the data is applied to the Green's functions. To estimate the maximum allowable rupture speed, we perform multiple experiments using several different rupture speeds and analyze the corresponding changes on the data fit. The results (Ⓔ Fig. S6) indicate different datasets are well fit when a fast rupture speed of 3.4–3.6 km/s is adopted. We thus fix 3.4 km/s as the maximum rupture speed in the inversion.

Relative data weighting presents a tricky issue in the joint inversion (Yue and Lay, 2013). In this study, we normalize each data type by its own norm and test different weighting factors. We find that a simple equal weighting can fit all datasets reasonably well. As a result, we assign all different data types to be equally weighted. Specially, coseismic GPS offsets at many sites are less than 0.5 cm and around the detection precision level of GPS technology, we set weights of < 0.5 cm GPS displacements to be 1/10. Joint inversion of the GPS, InSAR, and teleseismic *P*-wave datasets is conducted with a modified version of MudPy code originally developed by Melgar and Bock (2015).

Tsunami observations at two deep-ocean assessment and reporting of tsunami (DART) buoys and three coastal tide gauges (see their distribution in Fig. 6) from the National Oceanic and Atmospheric Administration's national data buoy center and Global Sea Level Observing System, respectively, are used to validate our preferred slip model. We use the seafloor displacements derived from the slip model as tsunami source and open-source code GeoClaw for the tsunami simulation. The model-predicted tsunami heights are compared with the observations. Publicly available topography and bathymetry data sets with 15 arc sec resolution (Becker *et al.*, 2009) are adopted for 6-hr tsunami propagation simulations.

Furthermore, using the ground-motion prediction equation (GMPE) proposed by García *et al.* (2005) which is specially developed for normal-faulting earthquakes in central Mexico, we computed the resulting PGAs based on our preferred slip model. Note that the adopted GMPE does not take into account site effects. As of this writing, no PGA data directly from strong-motion records are publicly available. For validation, we compare our synthetic PGAs with PGAs provided by USGS through ShakeMap (see Data and Resources) at selected stations.

RESULTS

Our preferred slip distribution and source time functions are shown in Figure 3, Ⓔ the model parameters are listed in the electronic supplement. The average strike, dip, and rake angles in our preferred model are ~318°, ~82°, and ~ − 94°, respectively. The peak slip is about 10 m at a depth of 50 km and the total seismic moment is 1.84×10^{21} N · m, equivalent to M_w 8.1. The variance reductions of 1 Hz GPS, static GPS, InSAR, and teleseismic waveform (Ⓔ Figs. S2–S5) from the best-fitting model are 42%, 51%, 64%, and 62%, respectively. The data fit to the InSAR data is not as good as in other earthquake cases, for example, the 2015 M_w 8.3 Illapel earthquake (e.g., Feng, Samsonov, *et al.*, 2017), because the InSAR observations used in this study are far from the source and SNR of the data is inherently low. The comparison of the simulated tsunamis and observations is shown in Figure 6. The model fits all data well, and the predicted tsunamis have good agreement with the observations.

As shown in Figure 3, the earthquake propagates as far as ~180 km toward the northwest along the strike, mainly unilaterally. The dominant slip of the earthquake is centered at ~40–50 km depth and ~65 km from the hypocenter. The $M_w > 4$ aftershocks seem to occur mostly above the main slip area. This may be related to coulomb stress changes in the shallow crust due to the mainshock although the uncertainties in aftershock locations could play a factor. The 3D view of the accumulated slip distribution (Fig. 3) shows the shallow slip occurs above the plate interface and into the overlying crust of the Cocos plate. We find that the shallow slip introduces more seafloor vertical displacements thus larger tsunami amplitude and provides a better fit to tsunami observations (Ⓔ Fig. S7). The main rupture takes place in the extensional regime in the oceanic lithosphere of the subducting Cocos plate, consistent with previous deep normal-faulting events in the region (Cocco *et al.*, 1997). Note that the source model from Okuwaki and Yagi (2017) using only *P*-wave data shows a quite compact and shallow slip distribution, however, these differences are likely caused by the limited resolution of teleseismic data.

Figure 4 depicts the spatiotemporal history of the earthquake rupture at 10 s intervals. The animation of the rupture process with 1-s interval is also provided in the Ⓔ Movie S1. The rupture initiates from the hypocenter, and expands along both dip and strike directions at fast speed (> 3 km/s). The rupture around the hypocenter reaches its down-dip limit in the first 10 s and then continuously propagates along strike to the northwest into the shallower depth. From 10 to 30 s, the main asperity is ruptured, during which the rupture process releases ~40% of the total seismic moment. From 30 to 40 s, the propagating rupture in the main asperity appears to pause

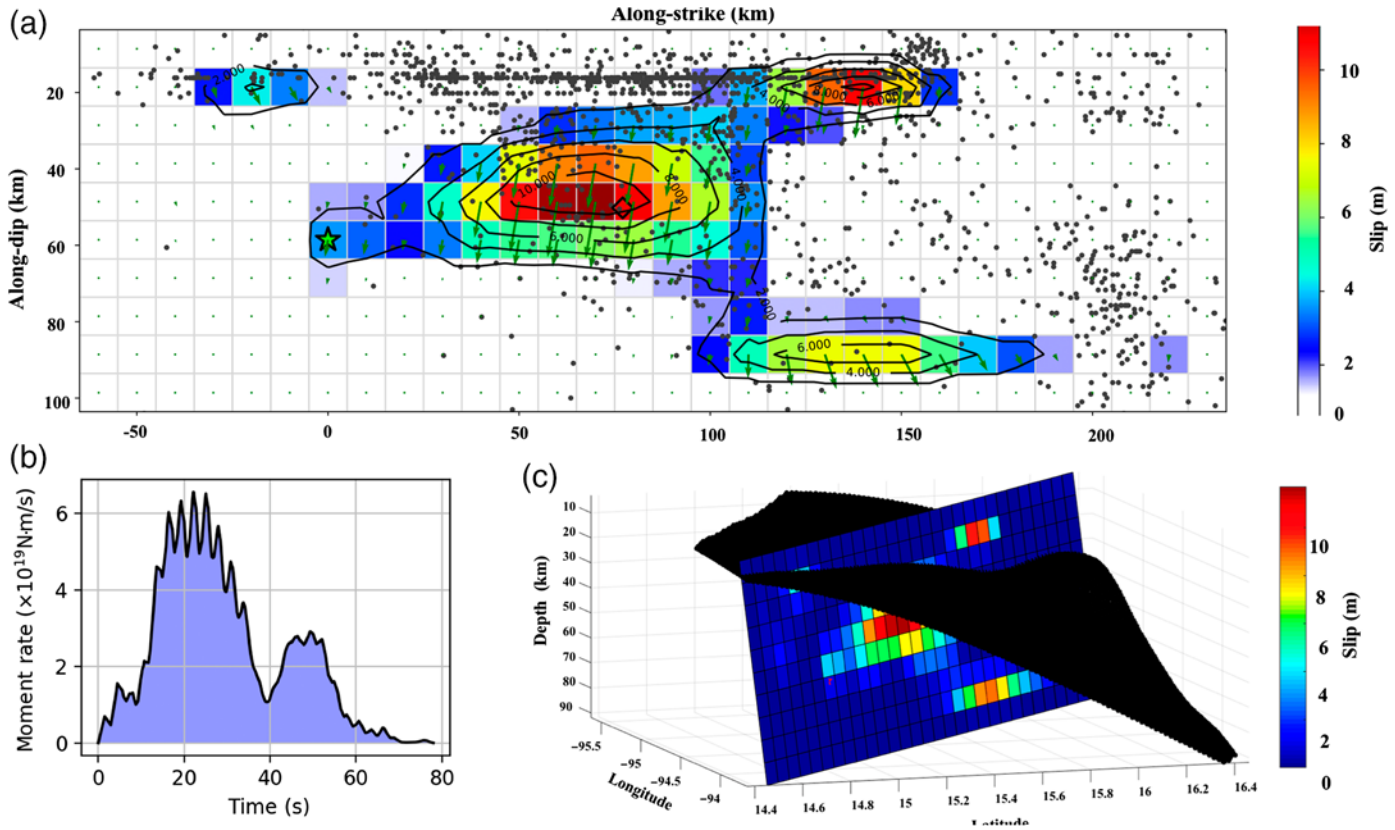

▲ **Figure 3.** (a) Tile view and (c) 3D view of the preferred slip distribution and (b) corresponding source time functions. The star denotes the hypocenter and gray dots are $M_w > 4$ aftershocks until 19 September 2017 from SSN. The diamond shows the location of the centroid of the Global CMT solution. The color version of this figure is available only in the electronic edition.

momentarily at ~110 km along the strike, then spread both up-dip and down-dip and continue to break into another two asperities at shallower (~20 km) and deeper (~90 km) depth. From 40 to 60 s, the earthquake rupture gradually terminates, with slip restricted in both shallow and deep slip zones. The abrupt change of rupture behaviors at ~110 km and the absence of continuing rupture at depths of ~40–50 km after 110 km may reflect a complex interaction between the earthquake rupture and pre-existing structural barriers in the region.

DISCUSSIONS

As mentioned in the Introduction, the 2017 M_w 8.1 Tehuantepec earthquake has triggered strong ground motions as far as in Mexico City, at an epicentral distance of ~720 km. The synthetic and observed PGAs are shown in Figure 5. As we can see, within distance < 300 km, GMPE by García *et al.* (2005) predicts PGA quite reasonably except one outlier. The outlier may be caused by strong site effects because that station is located in a very soft soil with V_{S30} around 200 m/s. However, as distance grows, GMPE seems to underestimate PGA systematically. In this regard, it has been well recognized that the sediment layer in Mexico City can amplify shaking there (Beck and Hall, 1986). Besides, for this special event, our slip model reveals that majority of the slip is in deep low-attenuation mantle, which indicates enriched short-period energy (Melgar *et al.*, 2016; Ye *et al.*, 2017), durable shaking, and larger angle of incidence. Effects of earthquake rupture directivity have been reported to enhance strong shaking as well but such effects are most common in strike-slip and thrust-slip events (Koketsu *et al.*, 2016) and very rare in normal-faulting earthquakes. To test if the rupture propagation revealed in our kinematic slip model has any effect on the observed strong motion at the surface, we examined dynamic displacements at two GPS stations: SSIA and KVTX (see their locations in Fig. 2). Although SSIA (with ~600 km epicentral distance opposite rupture direction) is much closer than KVTX (with ~1450 epicentral distance along rupture direction) to the epicenter, it shows relative weaker dynamic displacements (see Ⓔ Figs. S8 and S9). KVTX is anchored to bedrock by a deep-drilled bedrock monument, which implies that it is free from site effects. Our PGA calculation and contrasting behaviors of the two sites suggest that the directivity may play a significant role in affecting the observed surface ground displacement.

The Tehuantepec earthquake is notable in its triggering of a large-scale tsunami warning, but no damaging waves were observed. The cautious warning seems consistent with the earthquake characteristics, such as the large magnitude, normal faulting, and near-shore location. However, the deep slip may weaken the tsunami potential, whereas the part of the shallow

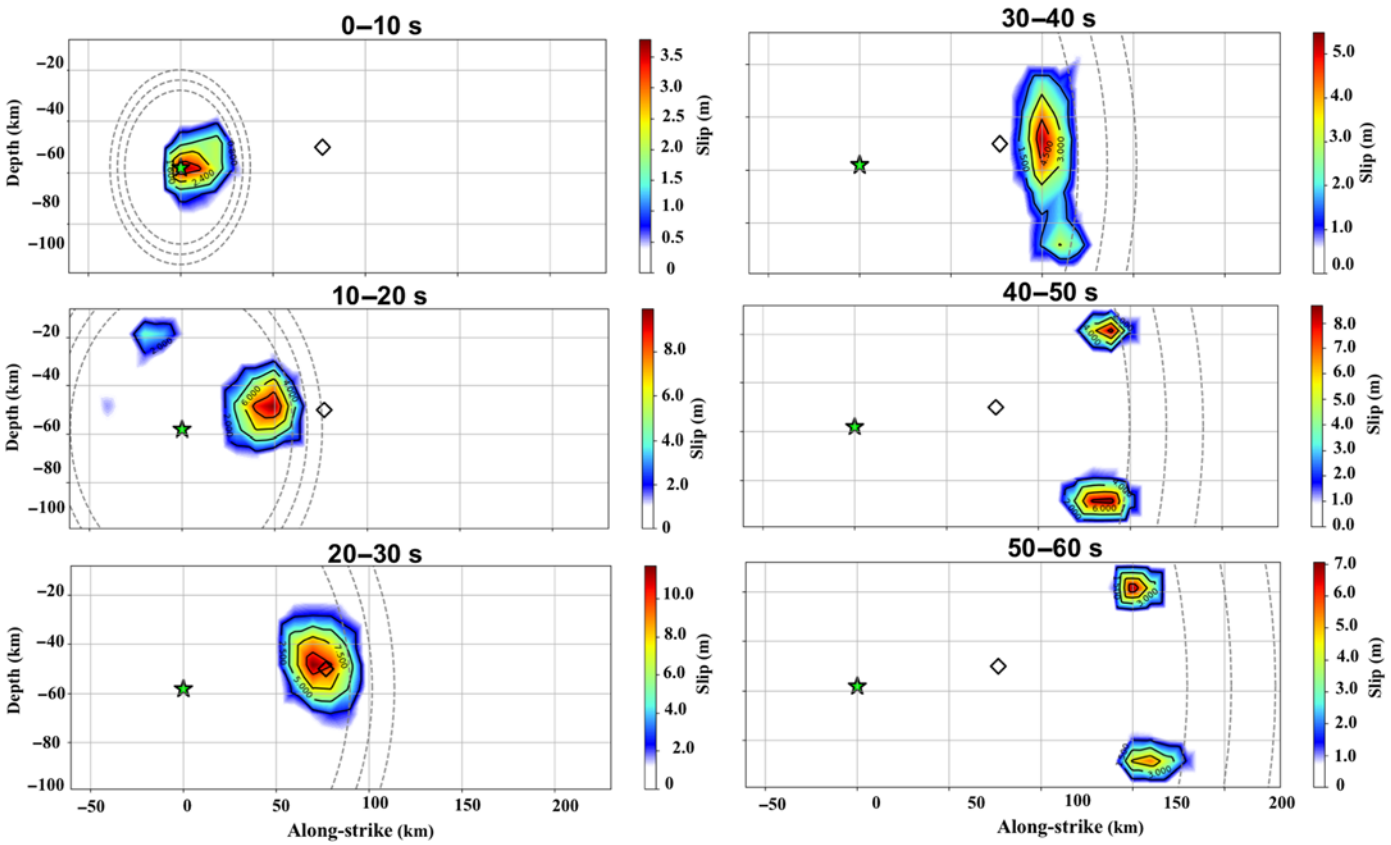

▲ **Figure 4.** Snapshots of the space-time history of the rupture propagation in 10 s intervals. The star is the hypocenter and diamond is the centroid location of the Global CMT fault solution. Gray dashed lines are reference rupture fronts moving out at 3.0, 3.4, and 3.8 km/s. To illustrate slip evolution clearly, each subplot has its own color scale. The color version of this figure is available only in the electronic edition.

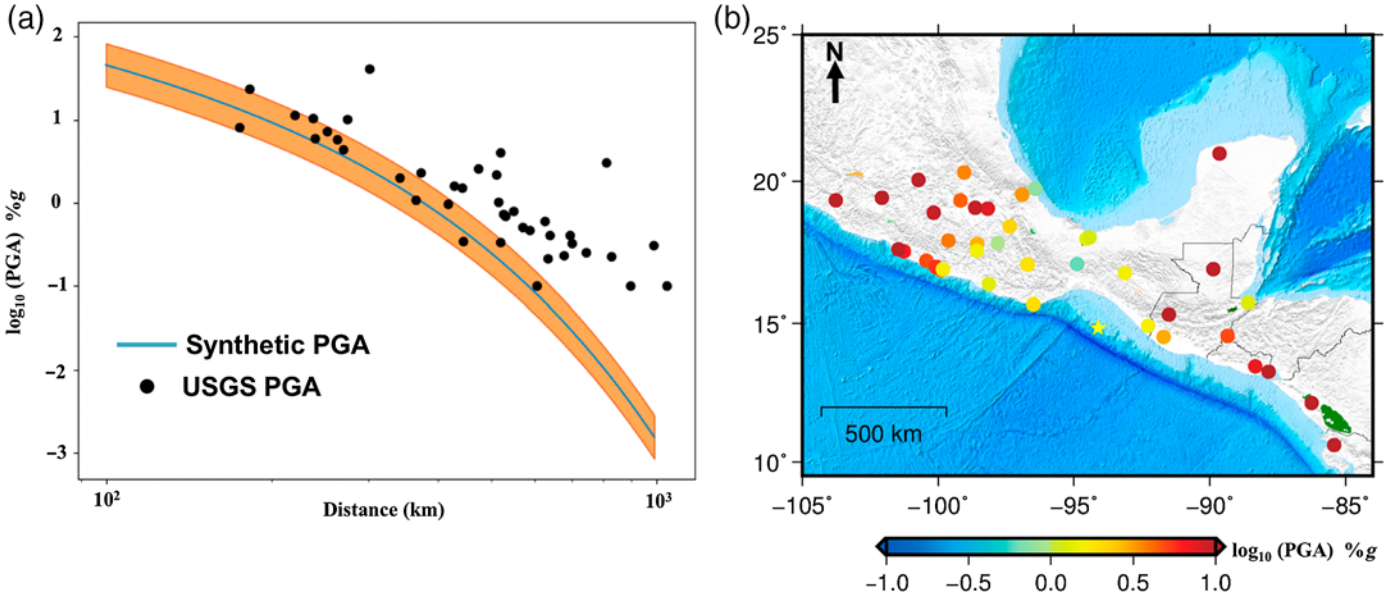

▲ **Figure 5.** (a) Synthetic (line) and USGS peak ground accelerations (PGAs) (dots), the shaded area denotes the synthetic PGA's standard deviation and (b) PGA residuals (USGS–synthetic). The star denotes the epicenter provided by SSN and dots show residuals at specific locations. The color version of this figure is available only in the electronic edition.

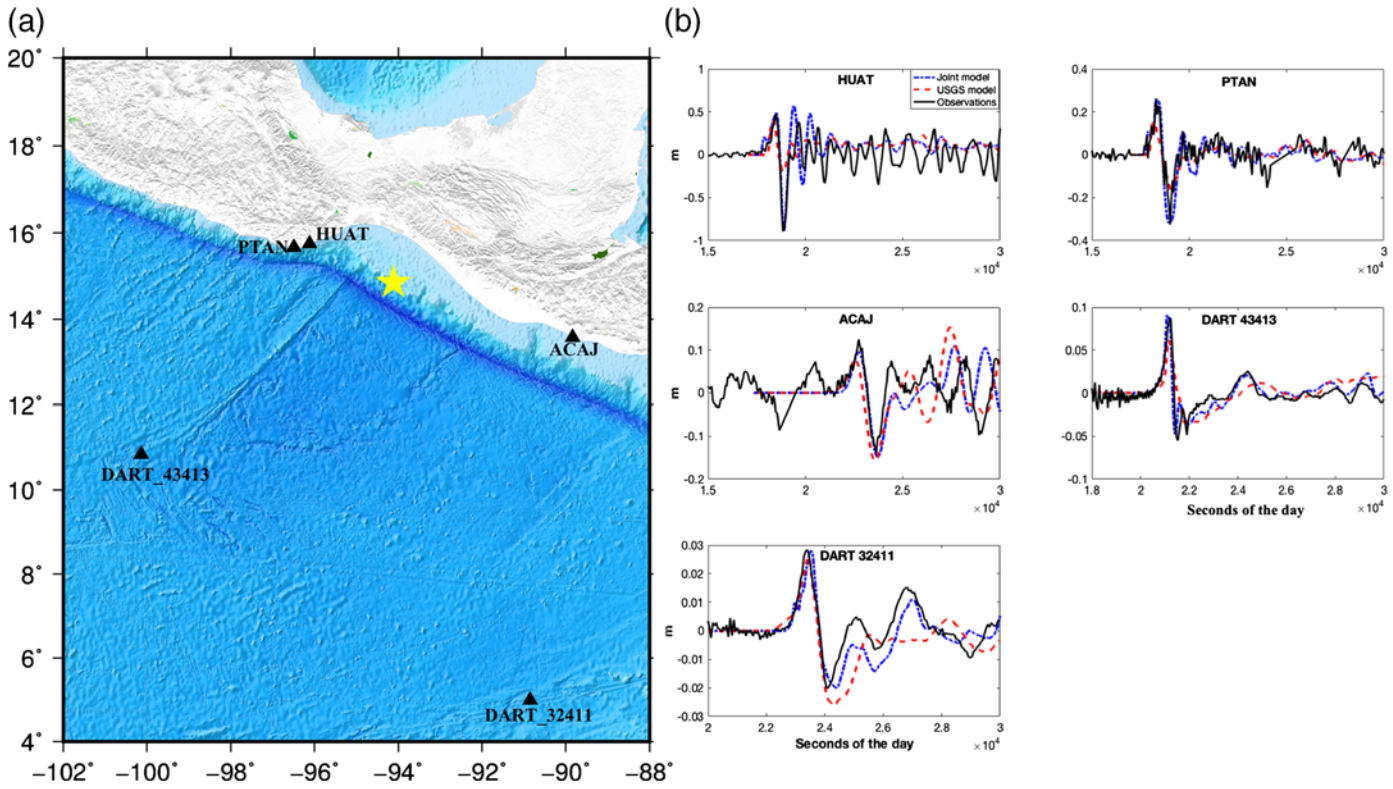

▲ **Figure 6.** (a) Distribution of deep-ocean assessment and reporting of tsunami (DART) buoys and near coastal tide gauges. (b) Tsunami observations (solid line), predictions (dashed–dotted line) from our preferred slip distribution, and USGS slip model (dashed line). Note that the late coming tsunamis at coastal tide gauges are affected by wave reflections, which account for the misfits. The color version of this figure is available only in the electronic edition.

slip may contribute to the vertical sea floor displacements and the observed local tsunami amplitudes. To test this, we apply USGS slip model, which uses mainly teleseismic data and shows some similar slip features as ours (e.g., dominating unilateral propagation and total energy released), but with very little shallow slip. The unsolved shallow rupture in the USGS model is likely caused by the intrinsic limitation of spatial resolution by teleseismic data (Yue *et al.*, 2013). We run tsunami simulation based on the USGS result and find that it underestimates the maximum tsunami heights, especially for the local tide gauges (see Fig. 6). The findings highlight the importance of near-field data (e.g., high-rate GPS) in providing a more reliable tsunami hazard estimation in the subduction zones.

The time coincidence between the mainshock and aforementioned M_w 7.1 Puebla aftershock raises the question of whether they are interrelated. As is well recognized, big earthquakes will change surrounding crustal stress and increase the risk of seismic activity nearby (Hayes, 2016). Generally, it is believed that stress transfer effect is limited within the domain of three to four times the length of the main rupture. As shown in our slip model, the 8 September earthquake propagated about 180 km along the strike, which means that it may lead stress transfer as far as 500–700 km away. From this point, the 19 September event which has about 650 km epicentral distance, just lays in the gray zone of influence. However, because the details of earthquake triggering have not been fully understood yet, determination of explicit relationship between the two events requires more research work and is the topic of another study in the future.

CONCLUSIONS

We obtain a detailed rupture process of the 2017 M_w 8.1 Tehuantepec earthquake through a joint inversion using geodetic and seismic data and validate it with tsunami observations. Our results suggest that this mega-normal normal-faulting event is caused by the extensional strain release along a steep fault plane associated with slab bending in the subducting Cocos plate. The rupture of the mainshock propagates unilaterally at a relatively high rupture velocity, deep slip distribution and directivity effects are likely to enhance widespread shaking. There seems to be a strong barrier at depth from 40 to 60 km that forces the rupture propagation into shallower and deeper asperities. Whether the unruptured zone at depths of 40–60 km and ~110 km to the northwest of the hypocenter, as revealed in our model, will rupture in future earthquakes requires special attention and continuous monitoring. Including shallow slip improves the model fits to the tsunami observations, suggesting the shallow-slip feature is robust, implying that deep normal events can rupture to the

shallow crust which may intensify tsunami amplitudes. Our findings provide new insights into the cause of tsunami and earthquake hazards in central Mexico. Finally, the slip model allows for a more comprehensive analysis of the link between the 8 and 19 September earthquakes for future research.

DATA AND RESOURCES

The information about M_w 8.1 Tehuantepec and M_w 7.1 events from U.S. Geological Survey (USGS) is available at https://earthquake.usgs.gov/earthquakes/eventpage/us2000ahv0#executive and https://earthquake.usgs.gov/earthquakes/eventpage/us2000ar20#executive, respectively. Tsunami information can be found at http://ptwc.weather.gov/ptwc/text.php?id=pacific.TSUPAC.2017.09.08.1827. Finite source model of the M_w 8.1 Tehuantepec earthquake provided by USGS is at https://earthquake.usgs.gov/earthquakes/eventpage/us2000ahv0#finite-fault, and peak ground accelerations (PGAs) can be found at https://earthquake.usgs.gov/archive/product/shakemap/us2000ahv0/us/1509140917825/download/stationlist.txt. 1-Hz global positioning system (GPS) observations and static GPS offsets are achieved by Nevada Geodetic Laboratory (NGL) and publicly available at ftp://data-out.unavco.org/pub/highrate/, http://geodesy.unr.edu/news_items/Offsets_Pijijiapan_rapid24hr.txt, and geodesy.unr.edu/NGLStationPages/stations, respectively. Teleseismic *P* waves can be downloaded from the Incorporated Research Institutions for Seismology (IRIS) Data Management Center at http://ds.iris.edu/wilber3/find_stations/10402114. Interferometric Synthetic Aperture Radar (InSAR) observations are provided by European Space Agency (ESA). Tsunami records at deep-ocean assessment and reporting of tsunami (DART) buoys and coastal tide gauges are available at https://nctr.pmel.noaa.gov/Dart/ and http://www.ioc-sealevelmonitoring.org/map.php. Aftershocks information provided by National Seismological Service of Mexico (SSN) is available at http://www.ssn.unam.mx/sismicidad/ultimos. All websites were last accessed on December 2017.

ACKNOWLEDGMENTS

The research described here was conducted at the Jet Propulsion Laboratory, California Institute of Technology, under contracts with the National Aeronautics and Space Administration (NASA). The authors thank three anonymous reviewers and Associate Editor Brendan Crowell for their insightful comments. Valerie Sahakian, Brendan Crowell, and Diego Melgar gave us detailed instructions on the usage of ground-motion prediction equation (GMPE) to compute peak ground acceleration (PGA). Plotting and seismic data processing make use of Generic Mapping Tools (GMT) and Seismic Analysis Code (SAC) software packages. Our slip inversion codes are based on a modified open-source software package, MudPy. The authors thank European Space Agency (ESA) for providing the Sentinel-1 Terrain Observation by Progressive Scans (TOPS) synthetic aperture radar (SAR) data for free of charge.

REFERENCES

Aranda, J. M. E., A. Jimenez, G. Ibarrola, F. Alcantar, A. Aguilar, M. Inostroza, and S. Maldonado (1995). Mexico City seismic alert system, *Seismol. Res. Lett.* **66,** no. 6, 42–53, doi: 10.1785/gssrl.66.6.42.

Beavan, J, X. Wang, C. Holden, K. Wilson, W. Power, G. Prasetya, M. Bevis, and R. Kautoke (2010). Near-simultaneous great earthquakes at Tongan megathrust and outer rise in September 2009, *Nature* **466,** 959–963, doi: 10.1038/nature09292.

Beck, J. L., and J. F. Hall (1986). Factors contributing to the catastrophe in Mexico City during the earthquake of September 19, 1985, *Geophys. Res. Lett.* **13,** 593–596, doi: 10.1029/GL013i006p00593.

Becker, J. J., D. T. Sandwell, W. H. F. Smith, J. Braud, B. Binder, J. Depner, D. Fabre, J. Factor, S. Ingalls, S.-H. Kim, *et al.* (2009). Global bathymetry and elevation data at 30 arc seconds resolution: SRTM30_PLUS, *Mar. Geod.* **32,** 355–371, doi: 10.1080/01490410903297766.

Bird, P. (2003). An updated digital model of plate boundaries, *Geochem. Geophys. Geosys.* **4,** no. 3, doi: 10.1029/2001GC000252.

Chen, K., A. Babeyko, A. Hoechner, and M. Ge (2016). Comparing source inversion techniques for GPS-based local tsunami forecasting: A case study for the April 2014 *M* 8.1 Iquique, Chile earthquake, *Geophys. Res. Lett.* **43,** no. 7, 3186–3192, doi: 10.1002/2016GL068042.

Chen, K., M. Ge, A. Babeyko, X. Li, F. Diao, and R. Tu (2016). Retrieving real-time co-seismic displacements using GPS/GLONASS: A preliminary report from the September 2015 M_w 8.3 Illapel earthquake in Chile, *Geophys. J. Int.* **206,** no. 2, 941–953, doi: 10.1093/gji/ggw190.

Cocco, M., J. Pacheco, S. K. Singh, and F. Courboulex (1997). The Zihuatanejo, Mexico, earthquake of 1994 December 10 ($M = 6.6$): Source characteristics and tectonic implications, *Geophys. J. Int.* **131,** 135–145, doi: 10.1111/j.1365-246X.1997.tb00600.x.

Dziewonski, A. M., and D. L. Anderson (1981). Preliminary reference Earth model, *Phys. Earth Planet. In.* **25,** 297–356, doi: 10.1016/0031-9201(81)90046-7.

Farr, T. G., P. A. Rosen, E. Caro, R. Crippen, R. Duren, S. Hensley, M. Kobrick, M. Paller, E. Rodriguez, L. Roth, *et al.* (2007). The shuttle radar topography mission, *Rev. Geophys.* doi: 10.1029/2005RG000183.

Feng, W., K. Omari, and S. V. Samsonov (2016). An automated InSAR processing system: Potentials and challenges, *2016 IEEE International Geoscience and Remote Sensing Symposium*, 3209–3210.

Feng, W., S. Samsonov, Y. Tian, Q. Qiu, P. Li, Y. Zhang, Z. Deng, and K. Omari (2017). Surface deformation associated with the 2015 M_w 8.3 Illapel earthquake revealed by satellite-based geodetic observations and its implications for the seismic cycle, *Earth Planet. Sci. Lett.* **460,** 222–233, doi: 10.1016/j.epsl.2016.11.018.

Feng, W., Y. Tian, Y. Zhang, S. Samsonov, R. Almeida, and P. Liu (2017). A slip gap of the 2016 M_w 6.6 Muji, Xinjiang, China, earthquake inferred from Sentinel-1 TOPS interferometry, *Seismol. Res. Lett.* **88,** no. 4, 1054–1064, doi: 10.1785/0220170019.

García, D., S. K. Singh, M. Herraíz, M. Ordaz, and J. F. Pacheco (2005). Inslab earthquakes of Central Mexico: Peak ground-motion parameters and response spectra, *Bull. Seismol. Soc. Am.* **95,** no. 6, 2272–2282, doi: 10.1785/0120050072.

Hartzell, S., P. Liu, C. Mendoza, C. Ji, and K. M. Larson (2007). Stability and uncertainty of finite-fault slip inversion: Application to the 2004 Parkfield, California, earthquake, *Bull. Seismol. Soc. Am.* **97,** no. 6, 1911–1934, doi: 10.1785/0120070080.

Hayes, G. (2016). Seismology: Remote-controlled earthquakes, *Nat. Geosci.* **9,** 269–271, doi: 10.1038/ngeo2663.

Kikuchi, M., and H. Kanamori (1982). Inversion of complex body waves, *Bull. Seismol. Soc. Am.* **72,** 491–506.

Koketsu, K., H. Miyake, Y. Guo, H. Kobayashi, T. Masuda, S. Davuluri, M. Bhattarai, L. B. Adhikari, and S. N. Sapkota (2016). Widespread ground motion distribution caused by rupture directivity during the

2015 Gorkha, Nepal earthquake, *Sci. Rep.* **6,** no. 28536, doi: 10.1038/srep28536.

Lay, T., C. J. Ammon, H. Kanamori, Luis Rivera, K. D. Koper, and A. R. Hutko (2010). The 2009 Samoa-Tonga great earthquake triggered doublet, *Nature* **466,** 964–968, doi: 10.1038/nature09214.

Melgar, D., and Y. Bock (2015). Kinematic earthquake source inversion and tsunami runup prediction with regional geophysical data, *J. Geophys. Res.***120,** 3324–3349, doi: 10.1002/2014JB011832.

Melgar, D., and Y. Bock (2013). Near-field tsunami models with rapid earthquake source inversions from land- and ocean-based observations: The potential for forecast and warning, *J. Geophys. Res.* **118,** 5939–5955, doi: 10.1002/2013JB010506.

Melgar, D., W. Fan, S. Riquelme, J. Geng, C. Liang, M. Fuentes, G. Vargas, R. M. Allen, P. M. Shearer, and E. J. Fielding (2016). Slip segmentation and slow rupture to the trench during the 2015, M_w 8. 3 Illapel, Chile earthquake, *Geophys. Res. Lett.* **43,** no. 3, 961–966, doi: 10.1002/2015GL067369.

Okuwaki, R., and Y. Yagi (2017). Rupture process during the M_W 8.1 2017 Chiapas Mexico earthquake: Shallow intraplate normal faulting by slab bending, *Geophys. Res. Lett.* **44,** 1–8, doi: 10.1002/2017GL075956.

Payero, J. S., V. Kostoglodov, N. Shapiro, T. Mikumo, A. Iglesias, X. Pérez-Campos, and R. W. Clayton (2008). Nonvolcanic tremor observed in the Mexican subduction zone, *Geophys. Res. Lett.* **35,** no. 7, 1–6, doi: 10.1029/2007GL032877.

Santoyo, M. A., S. K. Singh, and T. Mikumo (2005). Source process and stress change associated with the 11 January, 1997 ($M_w = 7.1$) Michoacán, Mexico, inslab earthquake, *Geofis. Int.* **44,** 317–330.

Segou, M., and T. Parsons (2018). Testing earthquake links in Mexico from 1978 to the 2017 $M = 8.1$ Chiapas and $M = 7.1$ Puebla shocks, *Geophys. Res. Lett.* **45,** 708–714, doi: 10.1002/2017GL076237.

Sobolev, S. V., A. Y. Babeyko, R. Wang, A. Hoechner, R. Galas, M. Rothacher, D. V. Sein, J. Schröter, J. Lauterjung, and C. Subarya (2007). Tsunami early warning using GPS-Shield arrays, *J. Geophys. Res.* **112,** no. B08415, doi: 10.1029/2006JB004640.

Suárez, G., J. M. Espinosa-Aranda, A. Cuéllar, G. Ibarrola, A. García, M. Zavala, S. Maldonado, and R. Islas (2018). A dedicated seismic early warning network: The mexican seismic alert system (SASMEX), *Seismol. Res. Lett.* **89,** no. 2A, doi: 10.1785/0220170184.

Wang, S.-C., K. C. McNally, and R. J. Geller (1982). Seismic strain release along the Middle America Trench, Mexico, *Geophys. Res. Lett.* **9,** 182–185., doi: 10.1029/GL009i003p00182.

Ye, L., T. Lay, Y. Bai, K. F. Cheung, and H. Kanamori (2017). The 2017 M_w 8.2 Chiapas, Mexico, earthquake: Energetic slab detachment, *Geophys. Res. Lett.* **44,** 1–9, doi: 10.1002/2017GL076085.

Yue, H., and T. Lay (2013). Source rupture models for the M_w 9.0 2011 Tohoku earthquake from joint inversions of high-rate geodetic and seismic data, *Bull. Seismol. Soc. Am.* **103,** 1242–1255, doi: 10.1785/0120120119.

Yue, H., T. Lay, S. Y. Schwartz, L. Rivera, M. Protti, T. H. Dixon, S. Owen, and A. V. Newman (2013). The 5 September 2012 Nicoya, Costa Rica M_w 7.6 earthquake rupture process from joint inversion of high-rate GPS, strong-motion, and teleseismic P wave data and its relationship to adjacent plate boundary interface properties, *J. Geophys. Res.* **118,** 5453–5466, doi: 10.1002/jgrb.50379.

Zhang, Y., W. Feng, Y. Chen, L. Xu, Z. Li, and D. Forrest (2012). The 2009 L'Aquila M_W 6.3 earthquake: A new technique to locate the hypocentre in the joint inversion of earthquake rupture process, *Geophys. J. Int.* **191,** no. 3, 1417–1426, doi: 10.1111/j.1365-246X.2012.05694.x.

Zhang, Y., W. Feng, L. Xu, C. Zhou, and Y. Chen (2009). Spatio-temporal rupture process of the 2008 great Wenchuan earthquake, *Sci. China Earth Sci.* **52,** no. 2, 145–154, doi: 10.1007/s11430-008-0148-7.

Zhu, L., and L. A. Rivera (2002). A note on the dynamic and static displacements from a point source in multilayered media, *Geophys. J. Int.* **148,** 619–627, doi: 10.1046/j.1365-246X.2002.01610.x.

Kejie Chen
Zhen Liu
Y. Tony Song
Jet Propulsion Laboratory
California Institute of Technology
4800 Oak Grove Drive
Pasadena, California 91109 U.S.A.
Kejie. Chen@jpl.nasa.gov
Zhen. Liu@jpl.nasa.gov
yuhe.t.song@jpl.nasa.gov

Wanpeng Feng
Canada Center for Mapping and Earth Observation
Natural Resources Canada
Ottawa, Ontario
Canada K1A 0E4
wanpeng.feng@canada.ca

Published Online 30 May 2018